



Gas and liquid phase distribution and their effect on reactor performance in the monolith film flow reactor

A. K. Heibel^{a, *}, T. W. J. Scheenen^b, J. J. Heiszwolf^c, H. Van As^b, F. Kapteijn^c, J. A. Moulijn^c

^aCorning Inc., Corning, NY 14831, USA

^bWageningen NMR Centre, Department of Molecular Physics, Wageningen University, Dreijenlaan 3, 6703 HA Wageningen, The Netherlands

^cDelft ChemTech, Industrial Catalysis, Delft University of Technology, Julianalaan 136, 2628 BL Delft, The Netherlands

Abstract

Nuclear magnetic resonance imaging (MRI) has been applied to study the phase distribution in the monolith film flow reactor. The accumulation of the liquid in the corners of the square channel with an arc-shaped gas–liquid interface has been determined. The average liquid saturation is in good agreement with model calculations. Non-uniformities of the liquid distribution over the four corners of the square channel were apparent, besides the maldistribution over the cross-section of the monolith. Computational fluid dynamics (CFD) calculations applying the measured liquid distribution predict a broadening of the residence time distribution and a shorter break-through time, due to the maldistribution, which is in very good agreement with experimental results. The impact on the modeled gas–liquid mass transfer performance seems to be negligible, due to the nearly linear relation between $k_{GL}a_V$ and u_{LS} . © 2001 Elsevier Science Ltd. All rights reserved.

Keywords: Monolith; Two-phase flow; Film flow; Flow distribution; MRI; CFD

1. Introduction

Recently, the application of monolithic structures has been extended to multiphase gas–liquid–solid systems. Here two different flow regimes are the main focus of research. In Taylor or bubble-train-flow gas bubbles separated by liquid plugs pass through the individual channels of the monolith. Taylor flow monolith reactors can be operated in co-current up- and down-flow mode. A gas to liquid ratio between one and three is proposed to facilitate stable Taylor flow with superficial liquid velocities ranging from 0.05 to 0.15 m/s (Andersson, Irandoust, & Cybulski, 1998). Usually, monoliths with a channel diameter between 1 and 2 mm are applied.

On the other hand it is also feasible to operate the monolith reactor in the film flow regime. Here the liquid flows down the channel walls, whereas the gas occupies

the core of the channel. The separated flow passages of gas and liquid allow both co- and counter-current operation of the film flow monolith reactor. The channel dimensions usually range from 2 to 5 mm and superficial liquid velocities up to 0.05 m/s are applied with a gas to liquid ratio of up to 20.

Flow distribution is in general a concern in multi-phase reactors, due to the negative impact on reactor performance (Perry, Nutter, & Nutter, 1990; Bonilla, 1993). Many investigations for trickle-bed reactors (Wang, Mao, & Chen, 1998), packed columns (Marchot, Toye, Crine, Pelsser, & L'Homme, 1999) and structured packings (Fitz, King, & Kunesh, 1999) are documented in the literature. For the monolith reactor liquid distribution is even more important, due to the lack of mass transport perpendicular to the flow direction. On a macroscopic level the distribution of the fluids over the entire cross-section or all the channels is of interest. On a more microscopic level, the gas and liquid phase distribution in the individual channel is a vital input for a good mathematical description of the hydrodynamic and mass transfer phenomena.

* Corresponding author. Tel.: +1-607-974-8430; fax: +1-607-974-4431.

E-mail address: heibelak@corning.com (A. K. Heibel).

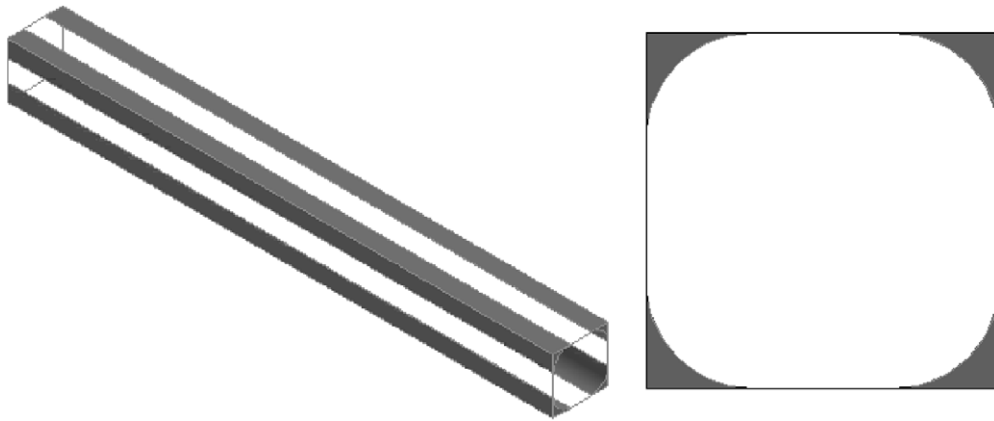


Fig. 1. Gas–liquid distribution in a square capillary in the film flow regime. Gray areas represent liquid accumulation in the corners.

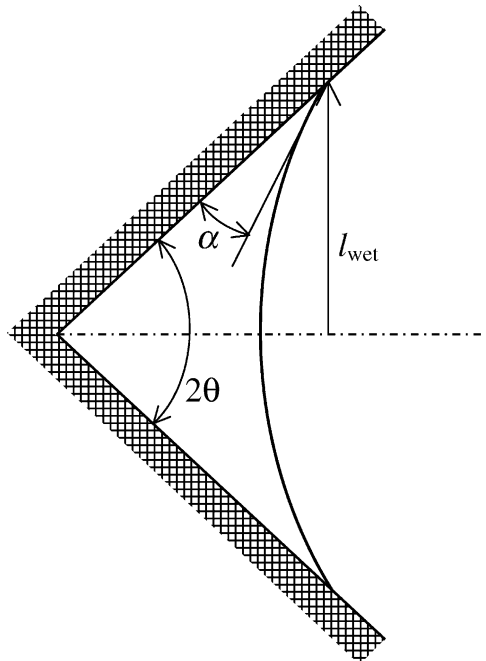


Fig. 2. Meniscus in an angled corner of a channel. Patterned area represents channel wall.

Several researchers have addressed the liquid and gas distribution in capillary size channels under film flow conditions. For a square shaped channel geometry the accumulation of the wetting fluid in the corners (Fig. 1) has been previously reported (Lenormand, Zarcone, & Sarr, 1983; Dong, Dullien, & Chatzis, 1995; Spildo & Buckley, 1999). In these studies the effect of gravity was neglected. According to Dong et al. (1995) spontaneous imbibition of the wetting liquid occurs in the corner of channels with acute angles. The resulting curvature (C_{wet} , Fig. 2) is dependent on the corner angle of the channel (2θ), the contact angle at the contact line (α) and the shortest distance between the two liquid–solid contact

lines ($2l_{\text{wet}}$):

$$C_{\text{wet}} = \frac{\cos(\theta + \alpha)}{l_{\text{wet}}}. \quad (1)$$

For square channels ($\theta = 45^\circ$) and complete wetting ($\alpha = 0^\circ$) the gas–liquid interface can be therefore defined with the inscribed quarter of a circle (r_{wet}) in the channel corner (Fig. 1).

$$r_{\text{wet}} = \sqrt{2}l_{\text{wet}}. \quad (2)$$

Kolb (1993) investigated experimentally the gravity driven two-phase flow in capillaries, which also confirmed the corner flow phenomena. These flow characteristics were successfully implemented in a hydrodynamic model for the monolith reactor with internally finned channels by Lebens, Stork, Kapteijn, Sie, and Moulijn (1999) and showed good agreement with experimental results.

Different non-destructive methods have been utilized to investigate the hydrodynamics in multiphase reactors based on conductance, capacitance, optical and X-ray tomography (Chaouki, Larachi, & Dudukovic, 1997). Recently, nuclear magnetic resonance imaging (MRI) has been applied to determine the flow field, the phase distribution and mass transfer phenomena in packed beds (Seymour & Callaghan, 1997; Tallarek, van Dusschoten, Van As, Guiochon, & Bayer, 1998; Manz, Gladden, & Warren, 1999; Mantle, Sederman, & Gladden, 2001). The aim of this work is to investigate the two-dimensional phase distribution of gas and liquid over the cross-section of the monolith (monolith-scale) and in the individual channel (channel-scale) by MRI. Besides the qualitative information about the shape of the gas–liquid interface and the location of the liquid, quantification of the mean liquid hold-up and its variations are of interest. Furthermore, the description of the flow field with a hydrodynamic model and the impact of local flow non-uniformities on residence time distribution and gas–liquid mass transfer are assessed.

2. Principles of NMR imaging

^1H -nuclei possess a quantum mechanical property called spin, which is classically presented as a small magnetic moment. When placed in a magnetic field, spins precess around the magnetic field vector at a frequency (the Larmor frequency) that depends on the magnetic field strength (Farrar & Becker, 1971) and the characteristic gyromagnetic ratio of the observed nucleus (in this case a proton). The small difference in energy level between spins precessing along the magnetic field vector (spin up) and spins precessing opposite to the magnetic field vector (spin down) causes a thermally equilibrated surplus of spins along the magnetic field resulting in a net magnetization vector of the spins along the magnetic field axis. This net magnetization vector can be manipulated by disturbing the equilibrium of the nuclear spin system with radio frequency (RF) pulses, produced with an RF coil around the protons in the magnetic field ('excitation'). Magnetization in the plane perpendicular to the magnetic field after excitation induces a RF signal (or NMR signal) in the coil around the sample. The magnetization vector will return to its initial size and direction with two typical time constants: the spin–spin relaxation time (T_2) characterizes the loss of magnetization in the plane perpendicular to the magnetic field (which is the loss of the NMR-signal), whereas the return of magnetization along the magnetic field is characterized by the spin–lattice relaxation time (T_1).

The NMR-signal, representing the magnetization in the plane perpendicular to the magnetic field axis, is a vector with an amplitude and phase, precessing at the Larmor frequency. Linear magnetic field gradients, superimposed on the static magnetic field, generate a position-dependent Larmor frequency: different frequencies of the NMR-signal can be processed (by a Fourier transform) into an NMR image, which is a map of the NMR-signal for every position in a sample. Multi-echo MRI (Edzes, van Dusschoten, & Van As, 1998) samples the NMR-signal in time for every pixel in a so-called echo-train. The decay of the NMR-signal ($S(t)$) in time (t) can be fitted to a mono exponential function:

$$S(t) = A_0 e^{-t/T_2} \quad (3)$$

in which A_0 is the calculated amplitude of the signal at the moment of excitation, which represents the spin density (or water density) of the corresponding pixel in the image, and T_2 is the corresponding spin–spin relaxation time.

3. Experimental

A 25 cells per square inch (cps) monolith with square channels of a hydraulic diameter of 4.11 mm and a length of 500 mm was used for the experiments. A custom made distribution section was connected on the top of the

monolith, using a $\varnothing 45$ mm Acrylate tube. The monolith material is cordierite ($2\text{MgO} \cdot 2\text{Al}_2\text{O}_3 \cdot 5\text{SiO}_2$) with a bulk porosity of around 30%. For the channel-scale experiments the outer channels were removed over $\frac{2}{3}$ of the monolith length and only four channels (2×2) in the center were kept over the entire length. The liquid flowing out of the outer region was drained by inserting Tygon[®] tubes in the individual channels. This experimental arrangement allowed to perform the channel-scale measurements with the wetting properties of the cordierite material on the one hand and the application of the standard liquid distribution section on the other hand. Furthermore, a high enough resolution to determine the phase distributions in the individual channels is obtained. The outer skin was sealed with a polymeric resin to prevent leakage to the outside. The liquid and gas phase consisted of water and air, respectively. All measurements were performed at room temperature and ambient pressure. The water was doped with small amounts of MnCl_2 (0.2 mmol/l) to decrease NMR relaxation times, so repetition times can be shorter and the total measurement time decreases. No forced gas flow was applied in the experiments, however free suction of gas was possible. Three different liquid distributors were used to cover the liquid flow range of interest. A gear pump (Micropump, Series 223) circulated the liquid and the flow was measured via a turbine flow sensor (Digi-flow systems, DFS-2, $\pm 1\%$ full scale). Prior to the tests the distributors have been tested on a cold-flow liquid distribution test bench to determine the optimum nozzle position (Heibel, Heiszwolf, Kapteijn, & Moulijn, 2001). The prepared monolith with the connected distribution section was mounted into the NMR imager (Fig. 3).

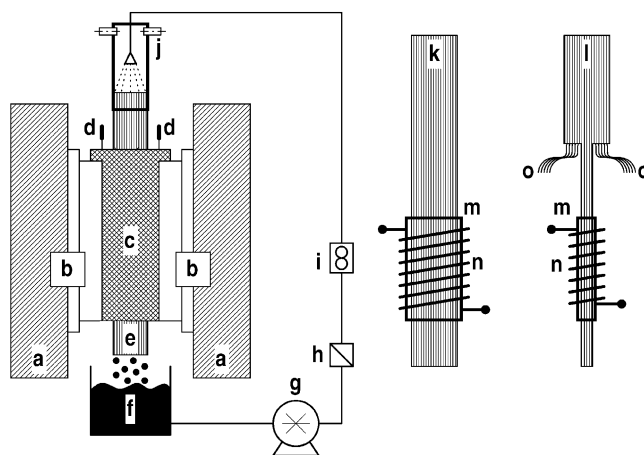


Fig. 3. MRI setup for monolith testing. (a) Magnet poles; (b) pole caps; (c) gradient and RF coil housing; (d) tuning and matching; (e) monolith test section; (f) liquid collection vessel; (g) pump; (h) strainer; (i) flow meter; (j) liquid distribution section; (k) monolith-scale test section; (l) channel-scale test section; (m) glass tube; (n) RF coil; (o) drainage tubes.

4. Hydrodynamic and diffusion model

A hydrodynamic model (Heibel et al., 2001) for the single channel was established based on the Navier–Stokes equation and the following assumptions:

- fully developed laminar flow in the gas and liquid phase;
- liquid accumulation in the corners;
- arc-shaped gas–liquid interface (Fig. 1) and
- contact angle of 0° at the gas–liquid–solid contact line (Eq. (2)).

With these considerations the Navier–Stokes equations reduce to a Poisson equation:

$$\nabla \cdot (\eta \nabla u_{F,z}) = -\frac{dp}{dz} + g \cdot \rho. \quad (4)$$

The cross-section of a channel was split into a gas and a liquid section and the no-slip boundary conditions at the wall ($u_z = 0$) and at the gas–liquid interface ($u_{G,z} = u_{L,z}$) were imposed. The differential form of the mass balance was used for the modeling of the mass transfer and residence time distribution studies. Only the liquid phase was considered in these simulations. The result of the flow field calculation (Eq. (4)) is a necessary input in the convection term for the calculation of the concentration field.

$$\frac{\partial c}{\partial t} + u_{L,z} \cdot \frac{\partial c}{\partial z} = \nabla \cdot (D \nabla c). \quad (5)$$

A zero-flux boundary condition was applied at the wall and the gas–liquid interface. For the residence time distribution calculation a transient analysis was performed with applying a step change at the inlet and monitoring the response at the outlet. The gas–liquid mass transfer performance was calculated with steady-state simulations. Different than for the residence time distribution model fully saturated liquid was assumed at the gas–liquid interface ($c = 1$). The physical absorption of oxygen in water has been chosen for the calculations. A summary of the physical properties is given in Table 1.

The partial differential equations were solved using the finite element (FEM) and the finite volume (FV) method. The symmetry of the channel allowed modeling of only one-eighth of the domain.

Table 1
Fluid properties at 20°C and 1.015 bar_a (Janssen & Warmoeskerken, 1991)

	Water	Air
Density (kg/m ³)	998	1.2
Dyn. viscosity (Pa s)	1.00×10^{-3}	1.82×10^{-5}
Diffusivity (m ² /s)	2.05×10^{-9a}	2.3×10^{-9b}

^aSelf-diffusion of water (Weingärtner, 1982).

^bOxygen in water.

5. Results and discussion

5.1. Monolith-scale experiments

The calculated NMR images (A_0 from Eq. (3)) of the whole monolith show three distinct regions (Fig. 4): the gas region in the center (no amplitude), the flowing liquid in the corners of the channels (high amplitude) and the trapped liquid in the walls (low amplitude). Two effects cause the low liquid density in the wall areas. On the one hand the maximum liquid hold-up in the wall is restricted by the material porosity (30%), so that the actual water density is much lower compared to the filled area in the channel. On the other hand the water molecules in the wall have a very short T_2 -value, due to the interaction with the surrounding solid structure. Therefore, the fit to the mono-exponential function is not accurate, since only one or two echoes contain signal. Under the applied film flow operation the preferential flow of the liquid in the corners ('corner flow') of the channel is clearly visible. In general, a good liquid distribution is observed especially for distributor B and C, which is in agreement with the cold flow distribution testing. For distributor A both test methods resulted in a liquid deficiency in the center of the monolith, which gives additional confidence in the experimental techniques. Furthermore, the images imply, that higher liquid velocities result in a higher liquid hold-up. Additionally, differences in the size of the liquid pockets in a single channel can be determined, but a higher resolution is necessary to allow for quantitative conclusions. The distortions in the amplitude images are caused by the non-linearity of the magnetic field gradient (especially on the bottom left-hand side of the images). These distortions were experienced throughout all measurements with large field of view (50 mm).

5.2. Channel-scale experiments

To assure a proper representation of the geometric proportions by the MRI technique two stagnant liquid measurements with a precision $5\text{ mm} \times 5\text{ mm}$ square and $\varnothing 3.98\text{ mm}$ round glass capillary as phantom geometries were performed. The qualitative analysis of the results (Fig. 5) shows very good agreement between the real geometry and the image. For the quantitative analysis the ratio of the sum of pixels from the two images is compared to the real void area fraction of the assembly of the two capillaries. The relative values of 50.9% for the image and 50.2% for the real geometry are in very good agreement.

Similar observations compared to the monolith-scale experiments (Fig. 4) concerning the liquid phase location are made for the four channel experiments (Fig. 6a); however, with much higher resolution. Again the liquid in the porous walls is detected with a lower intensity, due

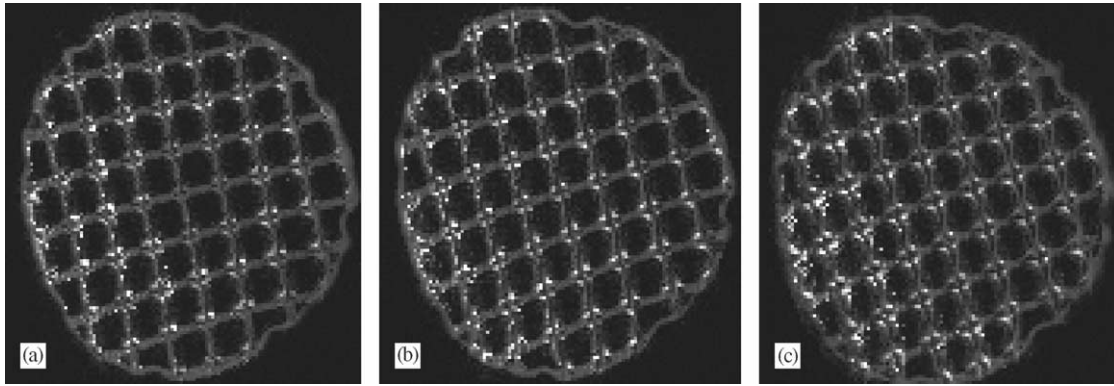


Fig. 4. Monolith-scale MRI images, bright colors represent high liquid density, dark colors represent low liquid density, black color represents gas phase. (a) $u_{LS} = 0.75$ cm/s distributor A; (b) $u_{LS} = 0.95$ cm/s distributor B; (c) $u_{LS} = 2.25$ cm/s distributor C. Parameters for the MRI experiments: magnetic field strength 0.47 T, image matrix 128×128 , field of view 50 mm, repetition time 1 s, no. averages 8, no. echoes 32, slice thickness 4 mm, first echo time 4.6 ms, echo time in train 4.2 ms, total measurement time 17 min.



Fig. 5. Validation experiments with stagnant fluid. (a) 5 mm square channel; (b) 5 mm square channel with $\varnothing 4$ mm round channel inserted. MRI parameters as in Fig. 4, except image matrix 192×192 , field of view 15 mm, repetition time 1 s, no. averages 4, no. echoes 32, slice thickness 4 mm, first echo time 6.0 ms, echo time in train 5.4 ms, total measurement time 13 min.

to the reasons mentioned above. The images are not distorted, because the magnetic field gradients were linear in the field of view of 15 mm.

For a better qualitative and quantitative analysis the original NMR images are post-processed. Basically, a minimum amplitude barrier has been defined, above which all amplitudes are regarded as 100% water. The barrier has been determined based on the real geometrical properties (l_w : wall thickness, d_h : hydraulic diameter) of the monolith compared to the one obtained from the image.

$$\left. \frac{l_w}{d_h} \right|_{\text{MRI}} \approx \left. \frac{l_w}{d_h} \right|_{\text{real}} \approx 21\%. \quad (6)$$

For all analyzed images the intensity barrier was very similar with a value between 0.125 and 0.165. This procedure masks the image of the porous wall and furthermore creates a somewhat crisper gas–liquid interface (Fig. 6a and b). Additionally some artifacts in the core of the channel are eliminated.

In Fig. 7 the effect of liquid flow rate is investigated for the three different distributors.

The liquid distribution over the channel corners is quite non-uniform for distributor A, while a more even distribution is obtained for B and C. The experimental results on a monolith-scale (Fig. 4) already revealed that distributor A has a zone of low liquid flow in the center of the monolith, which explains the odd behavior.

As a general trend an increase in liquid hold-up with increasing superficial velocity is determined. However, this relationship does not seem to be linear. The results clearly show the liquid accumulation in the corners. Furthermore, the gas–liquid interface exhibits an arc-shaped curvature and complete wetting seems to occur at the gas–liquid–solid contact line. These qualitative conclusions are in very good agreement with experimental and theoretical results of previous research (Kolb, 1993; Lebens et al., 1999).

Additionally, the results indicate that the liquid hold-up in the individual channel corners can still be substantially different, despite the liquid distribution homogeneity over the monolith cross-section.

For quantification the liquid saturation is considered, which is a function of the flow regime and the gas and liquid flow rates. The definition is given as the ratio between the liquid and the void area:

$$\beta_L = \frac{A_L}{A_L + A_G} = \frac{A_L}{A_V}. \quad (7)$$

In the film flow regime, only minor interaction between gas and liquid occurs at the gas–liquid interface, therefore the impact of the gas velocity on the liquid saturation is negligible, especially for the experiments with free suction. The superficial liquid velocity is defined based on the void area of the channel.

$$u_{LS} = \frac{\phi_L}{A_V n_{\text{ch}}}. \quad (8)$$

The ratio of the amount of pixels indicating liquid to the number of pixels required to cover the void of the channel determines the liquid saturation from the MRI

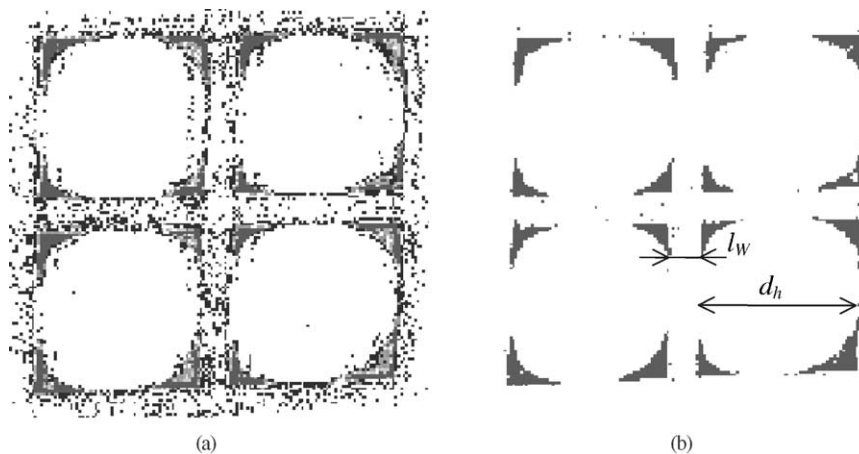


Fig. 6. (a) Original NMR image; (b) image after post-processing. MRI parameters same as in Fig. 5.

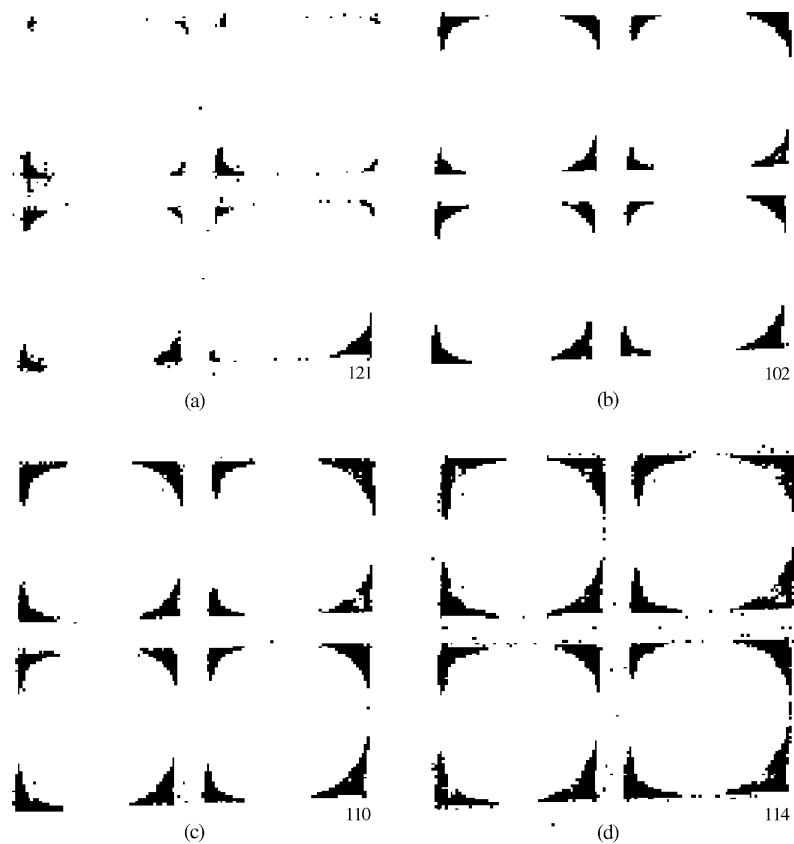


Fig. 7. Liquid phase distribution for different distributors and liquid velocities. (a) Distributor A, $u_{LS} = 0.45$ cm/s; (b) distributor B, $u_{LS} = 1.1$ cm/s; (c) distributor C, $u_{LS} = 2.2$ cm/s; (d) distributor C, $u_{LS} = 4.0$ cm/s.

experiments. A comparison with the results from the hydrodynamic model (Eq. (4)) as a function of superficial liquid velocity is illustrated in Fig. 8.

Good agreement between the average liquid saturation measured and the model estimate is obtained, which is also supported by previous work of Lebens et al. (1999) on finned monolith structures. Deviations towards

lower measured saturations are present for distributor A ($u_{LS} < 0.75$ cm/s). Again this is due to the maldistribution in the center region of the monolith as mentioned above. A good reproducibility of the measurements is given over the entire liquid flow range investigated, allowing the conclusion that the film is rather stable. Imposing liquid maldistribution on the monolith-scale

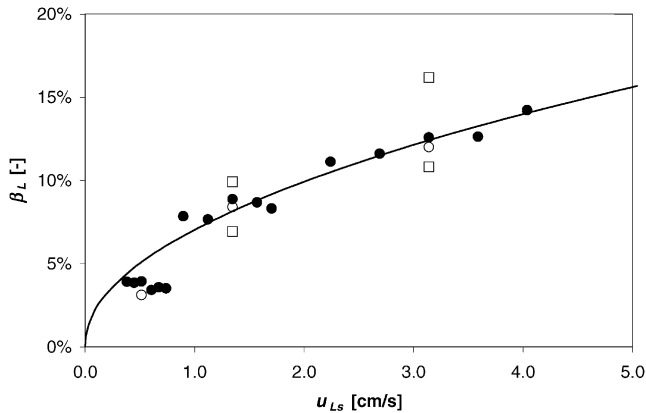


Fig. 8. Average liquid saturation as a function of the superficial liquid velocity. ● MRI measurement with optimum distributor position; ○ Repeat; □ MRI measurement with non-optimum distributor position; line represents model calculation.

by non-optimum positioning of the distributor results in deviations between modeled and measured liquid saturations, which is also confirmed by liquid-only distribution tests. An increase of the liquid saturation with superficial liquid velocity is apparent. However, this increase is non-linear and flattens out for higher liquid velocities. This behavior can be further investigated by studying the laminar flow field in channel direction with the hydrodynamic model (Fig. 9).

An increase of the superficial velocity by a factor of four results only in twice the liquid saturation, due to the higher velocities of the liquid in the area remote from the wall. They lead to an overall higher average film velocity resulting in a relatively lower liquid saturation.

Besides the average liquid saturation over all four channels, the MRI results allow also a more localized analysis. Therefore, the amount of pixels in the corner of

interest relative to the amount of pixels necessary to cover a quarter of the void of a channel is determined as the local liquid saturation (Fig. 10).

The average liquid saturation values are presented as dotted lines for the three superficial liquid velocities considered. The liquid saturation in one channel is evenly spread around the average, confirming a rather uniform distribution over the four channels. However, the individual corners in a channel show a wide variation in local liquid saturation values. These variations show a systematic behavior, independent of the liquid superficial velocity. A valid hypothesis might be that at the monolith entrance, where the corner flow starts to develop the geometry differs slightly and therefore more or less liquid is guided into a corner. The initial distribution propagates downstream, without the ability to redistribute, due to the stable nature of the liquid pockets in the corner.

6. Impact of distribution effects on reactor performance parameters

The actual liquid distribution as defined by the variations in local liquid saturation determined by the MRI experiments is used as input for modeling studies concerning some performance criteria of the monolith film flow reactor (i.e. the gas–liquid mass transfer and the residence time distribution). The values are compared to the predictions for a uniform distribution.

6.1. Gas–liquid mass transfer performance

A plug flow reactor model is assumed to calculate the average $k_{GL}a_V$ -value from modeling data, based on the

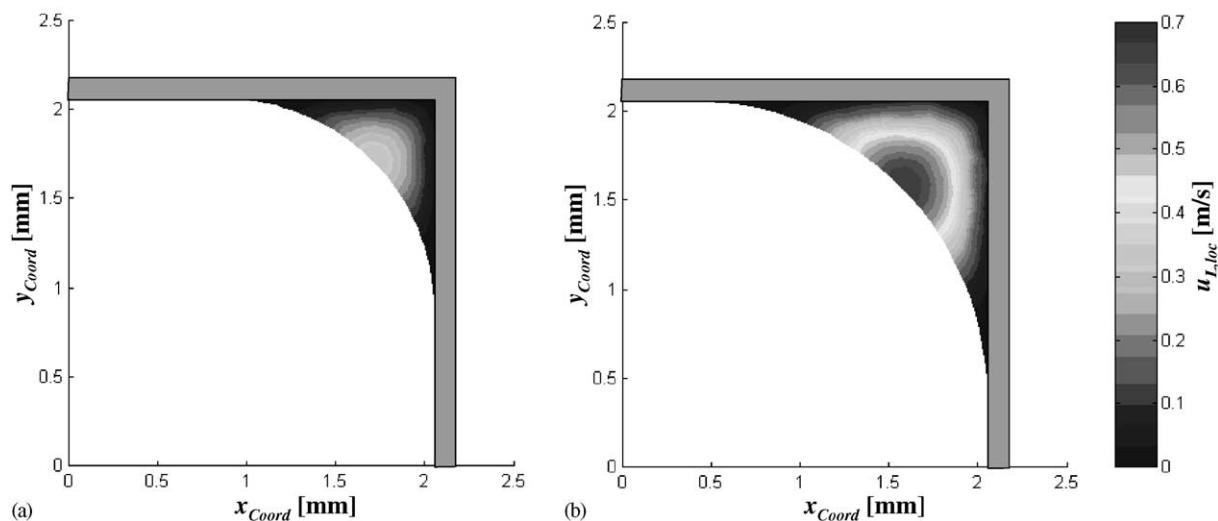


Fig. 9. Velocity field in one corner of the square channel as calculated by the hydrodynamic model (Eq. (4)). (a) $u_{LS} = 1.0$ cm/s, $\beta_L = 7\%$; (b) $u_{LS} = 4.0$ cm/s, $\beta_L = 14\%$, patterned area represents channel wall.

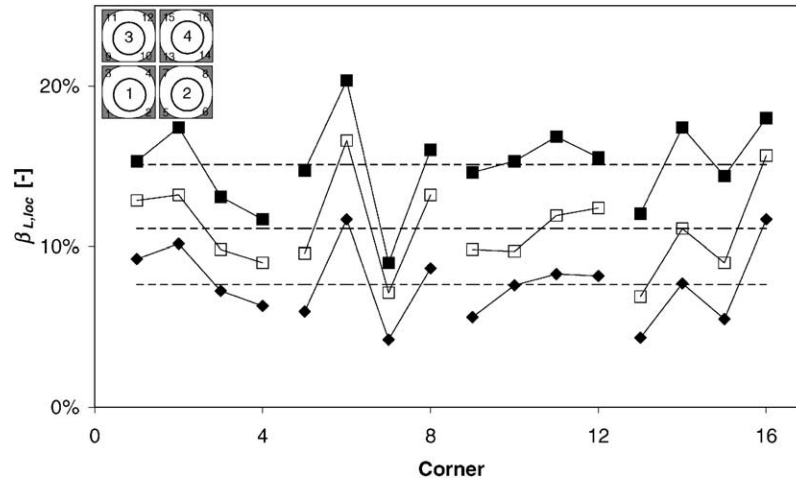


Fig. 10. Local liquid saturation in the individual corners for different superficial liquid velocities. \blacklozenge $u_{LS} = 1.1$ cm/s, \square $u_{LS} = 2.2$ cm/s, \blacksquare $u_{LS} = 4.0$ cm/s; dashed line represents average liquid saturation; first channel: corner 1–4; second channel: corner 5–8; third channel: corner 9–12; fourth channel: corner 13–16.

void fraction of the packing.

$$k_{GL}a_V|_l = \frac{u_{LS}}{l} \ln\left(\frac{c_{in}}{c_{mc,l}}\right). \quad (9)$$

The differences in local velocity have to be taken into account for the calculation of an average concentration, therefore the mixing-cup concentration is defined at the outlet (Zogg, 1971).

$$c_{mc,l} = \frac{\iint u_L(x,y)c_l(x,y) dx dy}{\phi_L}. \quad (10)$$

As reported previously (Heibel et al., 2001) the developing concentration profile at the inlet section has a significant contribution to the overall gas–liquid mass transfer. A monolith section of 500 mm has been chosen as a good representation for the model calculations.

The gas–liquid mass transfer shows an increase with liquid velocity mostly due to the increased gas–liquid contact area (Fig. 11). In general, somewhat lower values are predicted for the non-uniform distribution, but the difference is rather insignificant. This behavior is due to the slight non-linearity in the relationship between $k_{GL}a_V$ and u_{LS} , leading to a smaller gradient for higher liquid velocities. Furthermore, experimental data of Heibel et al. (2001) support the rather insignificant dependency of the gas–liquid mass transfer on channel-scale maldistribution.

6.2. Residence time distribution

Due to the fact that a step change from zero to a concentration of unity was applied at the inlet, the cumulative age distribution function (F_L) can be directly determined from the mixing-cup concentration at the outlet:

$$F_L(t) = c_{mc,out}(t). \quad (11)$$

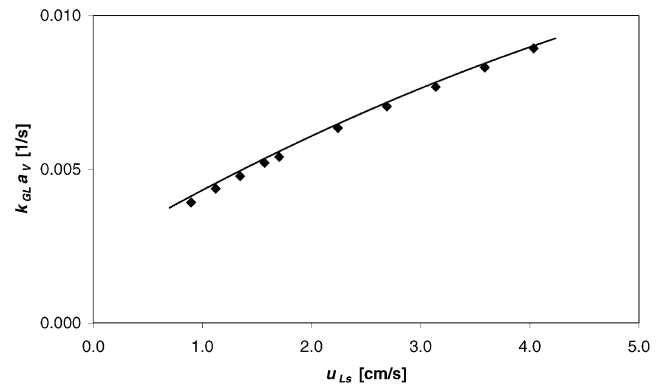


Fig. 11. Gas–liquid mass-transfer simulation results as a function of the superficial liquid velocities. \blacklozenge simulation results for maldistributed liquid flow over the 16 considered corners; line represents results for a uniform liquid distribution, oxygen/water at 20°C and 1 bar_a, 25 cpsi monolith, 500 mm long.

Table 2

Results of residence time distribution simulations with and without maldistribution. $u_{LS} = 2.25$ cm/s, air/water at 20°C and 1 bar_a, 25 cpsi monolith 500 mm long

	Actual RTD with maldistribution	Ideal RTD without maldistribution
Mean residence time— τ	2.22 s	2.37 s
Variance— σ^2	3.56 s ²	3.35 s ²
Break-through time— t_B	0.60 s	0.85 s

The exit age distribution function (E_L) follows by taking the derivative:

$$E_L(t) = \frac{dF_L(t)}{dt}. \quad (12)$$

The mean residence time and the variance are determined by the first and second moment of the exit age function, respectively (Table 2). Due to the channel-scale

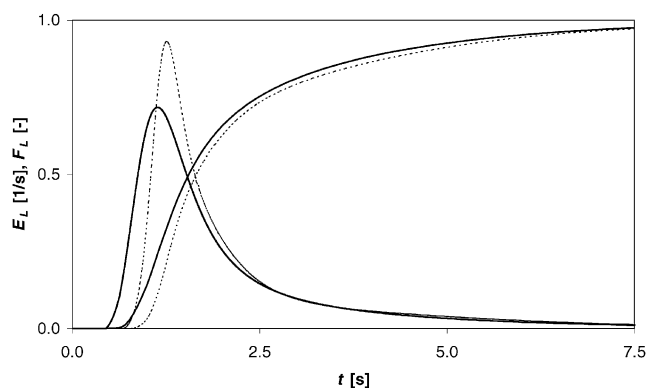


Fig. 12. Exit age distribution and cumulative exit age distribution as a function of residence time. Solid lines represent maldistributed flow; dashed lines represent uniform distributed flow, $u_{Ls} = 2.25$ cm/s, air/water at 20°C and 1 bar_a, 25 cpsi monolith, 500 mm long.

maldistribution effects a slight shift of the mean residence time occurs to lower values.

In Fig. 12 the simulated $F_L(t)$ and $E_L(t)$ curves are summarized for uniform and maldistributed flow. The higher local velocities in the laminar film of the corners with larger liquid pockets lead to an earlier break-through in the residence time distribution in the case of non-uniformities. Therefore, the residence time distribution curve is significantly shifted and broadened, which is indicated by the higher variance value. However, the tail of the distribution curve is still strongly dominated by the low velocities near the wall. In summary, this leads to more deviation from plug flow, which is undesired from a reactor performance standpoint.

Overall the simulation results are in good agreement with residence time distribution measurements on finned monoliths performed by Lebens (1999). His investigations showed that the experimental residence times are shifted to shorter times compared to the predicted values based on ideal liquid distribution, while a similar tailing of the distribution curve was detected. The current results, including the local liquid distribution in a monolith channel give an explanation for the differences between experimental data and model calculations based on uniform distribution.

7. Conclusions

Multi-echo nuclear magnetic resonance imaging (MRI) proved to be a useful tool to investigate the flow distribution on a monolith as well as a channel-scale in the two-phase film flow monolith reactor. In agreement with literature, the accumulation of the liquid in the corners of the square channels due to capillary forces is confirmed. An arc-shaped gas–liquid interface is determined.

Monolith-scale experiments allow a qualitative investigation of the macroscopic distribution differences over

the cross-section. With an appropriate choice of the distributor a rather uniform distribution of the liquid across the monolith is obtained, which is in good agreement with cold-flow liquid distribution testing. Higher resolution channel-scale measurements reveal, that also on a more microscopic level, significant liquid distribution differences over the corners of the individual channels are apparent. These variations show a systematic behavior, independent of the liquid velocity, and are therefore believed to result from geometrical differences.

The average liquid saturation is in very good agreement with CFD calculations based on the Navier–Stokes equations. Imposed maldistribution confirmed the expected trends in deviation of liquid saturation.

Simulation methods were applied to assess reactor performance parameters based on the determined variations in distribution. The gas–liquid mass transfer is rather insensitive to the channel-scale distribution differences. A more pronounced effect on the residence time distribution is calculated. Especially, the high local velocities in the corners of higher liquid saturation shift the break-through time to lower values and result in an overall broadening of the residence time distribution, which is not desirable from a reactor performance standpoint.

Notation

a	surface to volume ratio, m^2/m^3
A	area, m^2
A_0	initial amplitude, dimensionless
c	dimensionless concentration, dimensionless
C	curvature, m^{-1}
d_h	hydraulic diameter of the channel, m
D	diffusion coefficient, m^2/s
E	exit age distribution, s^{-1}
F	cumulative exit age distribution, dimensionless
g	gravitational constant, m/s^2
k	mass transfer coefficient, m/s
l	length, m
n_{ch}	number of channels, dimensionless
p	pressure, Pa
r_{wet}	radius of the gas–liquid interface curvature, m
S	NMR signal, dimensionless
t	time, s
T_1	spin–lattice relaxation time, s
T_2	spin–spin relaxation time, s
u	velocity, m/s
x, y, z	coordinate directions, m

Greek letters

α	gas–liquid–solid contact angle, dimensionless
β_L	liquid saturation, dimensionless
η	dynamic viscosity, $\text{Pa} \cdot \text{s}$
θ	half corner angle of the channel

ρ	density, kg/m ³
σ^2	variance of the residence time, s ²
τ	mean residence time, s
ϕ_L	volumetric liquid flow rate, m ³ /s

Subscripts

avg	average
<i>B</i>	break-through
ch	channel
<i>F</i>	fluid
<i>G</i>	gas
in	inlet
<i>L</i>	liquid
<i>l</i>	length
loc	local
<i>mc</i>	mixing cup
out	outlet
<i>s</i>	superficial
<i>V</i>	void
<i>w</i>	wall
wet	wetted
<i>x, y, z</i>	coordinate <i>x, y, z</i>

Acknowledgements

This work was in part supported by EC TMR Grant ERBFMGE-CT-950066 (access to EU large scale facility Wageningen NMR Centre) and Grant No. HPRI-CT-1999-00085 (EC programme Access to Research Infrastructure). Furthermore the authors like to thank Piet Lens for contributing some of the experimental time on the NMR imager at the Wageningen NMR Centre.

References

- Andersson, B., Irandoust, S., & Cybulski, A. (1998). Modeling of monolith reactors in three-phase processes. In A. Cybulski & J. A. Moulijn (Eds.), *Structured catalysts and reactors* (pp. 267–303). New York: Marcel Dekker Inc.
- Bonilla, J. A. (1993). Don't neglect liquid distribution. *Chemical Engineering Progress*, 89(3), 47–61.
- Chaouki, J., Larachi, F., & Dudukovic, M. P. (1997). Noninvasive tomographic and velocimetric monitoring of multiphase flows. *Industrial and Engineering Chemistry*, 36, 4476–4503.
- Dong, M., Dullien, F. A. L., & Chatzis, I. (1995). Imbibition of oil in film form over water present in edges of capillaries with angular cross section. *Journal of Colloid and Interface Science*, 172, 21–36.
- Edzes, H. T., van Dusschoten, D., & Van As, H. (1998). Quantitative T₂ imaging of plant tissues by means of multi-echo MRI microscopy. *Magnetic Resonance Imaging*, 16, 185–196.
- Farrar, T. C., & Becker, E. D. (1971). *Pulse and Fourier transform NMR*. New York: Academic Press.
- Fitz, C. W., King, D. W., & Kunesh, J. G. (1999). Controlled liquid maldistribution studies on structured packing. *Transactions of the Institution of Chemical Engineers*, 77, 482–486.
- Heibel, A. K., Heiszwolf, J. J., Kapteijn, F., & Moulijn, J. A. (2001). Influence of channel geometry on hydrodynamics and mass transfer in the monolith film flow reactor. *Catalysis Today*, accepted for publication.
- Janssen, L.P.B.M., & Warmoeskerken, M.M.C.G. (1991). Transport phenomena data companion, Delft: Delftse U.M.
- Kolb, W. B. (1993). *The coating of monolithic structures: Analysis of flow phenomena*. Ph.D. Thesis, The University of Tulsa.
- Lebens, P. J. M. (1999). *Development and design of a monolith reactor for gas-liquid countercurrent operation*. Ph.D. Thesis, Technical University of Delft.
- Lebens, P. J. M., Stork, M. M., Kapteijn, F., Sie, S. T., & Moulijn, J. A. (1999). Hydrodynamics and mass transfer issues in a countercurrent gas-liquid internally finned monolith reactor. *Chemical Engineering Science*, 54, 2381–2389.
- Lenormand, R., Zarcone, C., & Sarr, A. (1983). Mechanisms of the displacement of one fluid by another in a network of capillary ducts. *Journal of Fluid Mechanics*, 135, 337–353.
- Mantle, M. D., Sederman, A. J., & Gladden, L. F. (2001). Single- and two-phase flow in fixed-bed reactors: MRI flow visualization and Lattice-Boltzmann simulations. *Chemical Engineering Science*, 56, 523–529.
- Manz, B., Gladden, L. F., & Warren, P. B. (1999). Flow and dispersion in porous media: Lattice-Boltzmann and NMR Studies. *A.I.Ch.E. Journal*, 45(9), 1845–1854.
- Marchot, P., Toye, D., Crine, M., Pelsser, A.-M., & L'Homme, G. (1999). Investigation of liquid maldistribution in packed columns by X-ray tomography. *Transactions of the Institution of Chemical Engineers*, 77, 511–518.
- Perry, D., Nutter, D. E., & Nutter, A. H. (1990). Liquid distribution for optimum packing performance. *Chemical Engineering Progress*, 86(1), 30–35.
- Seymour, J. D., & Callaghan, P. T. (1997). A generalised approach to the measurement of flow and dispersion in a porous medium using nuclear magnetic resonance. *A.I.Ch.E. Journal*, 43, 2096–2111.
- Spildo, K., & Buckley, J. S. (1999). Uniform and mixed wetting in square capillaries. *Journal of Petroleum Science and Engineering*, 24, 145–154.
- Tallarek, U., van Dusschoten, D., Van As, H., Guiochon, G., & Bayer, E. (1998). Direct observation of fluid mass transfer resistance in porous media by NMR spectroscopy. *Angewandte Chemie International Edition*, 37, 1882–1885.
- Wang, Y.-F., Mao, Z. S., & Chen, J. (1998). Scale and variance of radial liquid maldistribution in trickle beds. *Chemical Engineering Science*, 53(6), 1153–1162.
- Weingärtner, H. (1982). Self diffusion in liquid water. A reassessment. *Zeitschrift fuer Physik alische Chemie*, 132, 129–149.
- Zogg, M. (1971). Der Stoffübergang an der freien Grenzfläche laminarer Rieselfilme. *Verfahrenstechnik*, 5(8), 328–333.